Microstructure and Creep Properties of Boron- and Zirconium-Containing Cobalt-based Superalloys

Peter J. Bocchini[a], Chantal K. Sudbrack[b], Ronald D. Noebe[b], David C. Dunand[a,b], David N. Seidman[a,c]

[a]*Department of Materials Science and Engineering, Northwestern University, 2220 Campus Drive, Evanston, Illinois 60208-3108, USA*

[b]*NASA Glenn Research Center, Materials and Structures Division*, 21000 Brookpark Rd., Cleveland, Ohio 44135, USA

[c]*Northwestern University Center for Atom-Probe Tomography (NUCAPT), 2220 Campus Drive, Evanston, Illinois 60208-3108, USA*

Abstract

The effects of micro-additions of boron and zirconium on grain-boundary (GB) structure and strength in polycrystalline γ(f.c.c.) plus γ'($L1_2$) strengthened Co-9.5Al-7.5W-X at. % alloys (X = 0-Ternary, 0.05B, 0.01B, 0.05Zr, and 0.005B-0.05Zr at. %) are studied. Creep tests performed at 850 ºC demonstrate that GB strength and cohesion limit the creep resistance and ductility of the ternary B- and Zr-free alloy due to intergranular fracture. Alloys with 0.05B and 0.005B-0.05Zr both exhibit improved creep strength due to enhanced GB cohesion, compared to the baseline ternary Co-9.5Al-7.5W alloy, but alloys containing 0.01B or 0.05Zr additions displayed no benefit. Atom-probe tomography is utilized to measure GB segregation, where B and Zr are demonstrated to segregate at GBs. A Gibbsian interfacial excess of 5.57 ± 1.04 atoms nm^{-2} was found for B at a GB in the 0.01B alloy and 2.88 ± 0.81 and 2.40 ± 0.84 atoms nm^{-2} for B and Zr, respectively, for the 0.005B-0.05Zr alloy. The GBs in the highest B-containing (0.05B) alloy exhibit micrometer-sized boride precipitates with adjacent precipitate denuded-zones (PDZs), whereas secondary precipitation at the GBs is not present in the other four alloys. The 0.05B alloy has the smallest room temperature yield strength, by 6 %, which is attributed to the PDZs, but it exhibits the largest increase in creep strength (with an ~2.5 order of magnitude decrease in the minimum strain rate for a given stress at 850 ºC) over the baseline Co-9.5Al-7.5W alloy.

1 Introduction

Co-base superalloys with the γ(f.c.c.) plus γ'($L1_2$) microstructure represent a new promising material class for alternatives to Ni-base superalloys[1-5] for high-temperature structural applications such as jet-engine turbine disks and blades. Conventional cobalt superalloys (e.g. Haynes 188[6]) are strengthened through solid-solution and/or carbide inclusion strengthening, rendering them useable in long-term applications at only modest temperatures, ~650 °C[2], however new cobalt superalloys based on the Co-Al-W system are strengthened by γ'($L1_2$)-precipitates embedded in a γ(f.c.c.)-matrix similar to Ni-based superalloys[7]. The synthesis of a Co-base superalloy with the γ(f.c.c.) plus γ'($L1_2$) microstructure has only recently been demonstrated in the Co-Al-W system [7-18], which was long thought to be unachievable based on the lack of a γ'($L1_2$) phase-field in Co-W and Co-Al binary systems.

The creep behavior of different single-crystal [11, 12, 19] and polycrystalline [16, 17, 20] γ(f.c.c.) plus γ'($L1_2$) Co-base superalloys has been studied to a degree. Polycrystalline ternary Co-Al-W alloys are, however, prone to fracture at their grain boundaries (GBs) during mechanical loading [13, 21]. Microalloying with B can promote the formation of GB borides, which increase GB cohesion and ductility, thereby increasing the creep strength of Co-alloys [17, 20]. A consequence of the precipitating borides is the formation of large precipitate-denuded zones (PDZs). PDZs have been shown to reduce yield strength in polycrystalline Ni-base superalloys [22] and therefore minimizing PDZ width is important for Co-alloy design. Shinagawa *et al.* [21] found that adding boron greatly enhances the yield strength of Co-base alloys through increased GB ductility, although in this case no GB borides were reported. GB strengthening in this situation was attributed to local segregation of B at GBs, analogous to results on polycrystalline Ni-based superalloys [23-25]. An added benefit of B is that it reduces oxidation rates in Co-superalloys by promoting the formation of a stable Al_2O_3-phase in the inner oxide layer at the alloy surface [26-29]. To date, B is the only GB strengthener that has been studied in γ(f.c.c.) plus γ'($L1_2$) Co-

base alloys, while the role of other GB strengtheners used in Ni-base superalloys, for example, Zr and C [23, 25, 30-32], have yet to be investigated.

In this research, different concentrations of B and Zr are studied as GB strengtheners in a ternary Co-9.5Al-7.5W alloy. Standard room temperature compression tests and Vickers microhardness measurements are utilized to determine the effects of B and Zr additions on yield strength. The effect of these GB additions on creep are evaluated employing compression creep tests at 850 °C for different constant loads. Atom-probe tomography (APT)[33, 34] is utilized to measure the concentrations of the trace elements B and Zr at GBs of selected γ(f.c.c.) plus γ'($L1_2$) Co-base superalloys[35]. Additional APT investigations are employed to measure the composition(s) of GB borides..

2 Experimental Procedures

Five button ingots with compositions Co-9.5Al-7.5W-X at. % (X = 0-Ternary, 0.05B, 0.01B, 0.05Zr, and 0.005B-0.05Zr at. %) weighing ~50 g were produced by arc melting high purity Co (99.9 %), Al (99.999 %), B (99.5 %), Zr (99.5 %) and a Co-9.5Al-7.5W master alloy cast by Sophisticated Alloys Inc., under a partial pressure of argon. Ingots were remelted 3-4 times, flipping the ingot between melts to ensure that all of the constituent elements were completely incorporated into the melt. The ingots were then homogenized in a vacuum furnace at 1300 °C for 24 h followed by furnace cooling to room temperature and subsequently heated to a supersolvus temperature of 1050 °C (60 °C higher than the solvus temperature of the γ'($L1_2$)-precipitates in ternary Co-Al-W[7]) for 6 h in an Ar atmosphere then dropped into sand and air-cooled. Final aging was conducted at 900 °C for 16 h in air and then air-cooled to obtain a γ(f.c.c.) plus γ'($L1_2$) microstructure.

Vickers microhardness measurements were performed at ambient temperature utilizing a Struers Duramin-5 microhardness tester with an applied load of 1 kg and a dwell time of 5 sec. Measurements

were made across multiple grains on samples that were polished to a 1 μm finish. Cylindrical compression samples with a 5 mm diameter and 10 mm length were cut from the aged buttons by electro-discharge machining and were used for ambient temperature compression tests and high-temperature compression creep tests. Samples for ambient temperature compression tests were sandwiched between tungsten carbide platens and deformed at a constant strain rate of 10^{-4} s^{-1} and deformed to 8 % plastic strain with a stress accuracy equivalent to ±15 MPa. Specimens for compression creep were sandwiched between two SiC platens lubricated with boron nitride. Compressive creep experiments were performed in air employing two dead-load creep frames, one equipped with a compressive load train and the other with a tensile load train in which a compression cage was inserted. The 0.05B and 0.01B alloys were tested using both frames to ensure compatible results, within expected experimental error. Samples used in the multi-stress creep tests were crept at 850 ± 2 °C as measured by a thermocouple placed within 1 cm of the sample. Displacements were measured by an extensometer connected to a linear variable displacement transducer with a resolution of 2.5 μm, yielding a minimum measureable strain increment of 2.5 x 10^{-4}. Strain rates were measured using the slopes taken from the strain vs. time curves. After a steady-state strain rate was observed and maintained over a sufficiently long period of time, the stress was increased to obtain the next minimum strain rate. The tests were terminated when the strain rate was observed to increase continuously for a given stress, indicating that the sample was failing.

Scanning electron microscopy (SEM) images and qualitative energy-dispersive X-ray spectroscopy (EDS) composition measurements were recorded using a Hitachi SU8030 and a Hitachi S-3400N-II SEM equipped with an Oxford INCAx-act SDD EDS detector. Samples used for SEM imaging were polished to a 1 μm finish and etched with a 1:1 solution of H_2O_2:HCl. The mean area equivalent radius (<R>) and the overall volume fraction (ϕ) for γ'-precipitates were measured by the line-intercept method [36] on SEM images taken close to a {100} plane. For an individual cuboidal γ'-precipitate, the

circular area-equivalent radius is calculated as $\sqrt{\frac{A}{\pi}}$, where A is the area as determined by measuring edge-lengths of the precipitates. The grain diameter (D) was measured by averaging grain areas (A_g) found by grain counting, and, assuming circular grains with an individual D = $\sqrt{\frac{4A_g}{\pi}}$.

Nanotip specimens used for selected-area APT studies of GBs were prepared using a Ga^+ dual-beam focused-ion beam (FIB) microscope lift-out technique utilizing a FEI Helios Nanolab SEM/FIB. Square-topped wedges (~2 μm^2) containing a GB were extracted from the Co alloys using the FEI dual-beam FIB microscope and were then attached to either a copper transmission electron microscopy (TEM) grid or a Si micropost on a coupon, and subsequently sharpened to a nanotips, using Ga^+ ions, to a ~50 nm radius. A dual-beam FIB ion energy of 5 keV and a current of 16 pA were used for the final sharpening stage. Due to the difficulty of resolving a GB in the nanotip in the dual-beam FIB microscope, the copper grid containing the nanotips were sometimes placed directly into a JEOL JEM-2100 FasTEM to check if the GB was in an acceptable volume of the nanotip for APT analyses. The APT specimens of the solutionized alloy were prepared by cutting parallelepiped blanks (~400 x 400 μm^2 cross-section). These blanks were then first electropolished with a rough-polish solution of 1:1 12.1 M concentrated hydrochloric:chromic acid, followed by a fine-polish solution of 2 % perchloric acid in butoxyethanol [37, 38]. APT was performed employing a Cameca 4000X-Si local-electrode atom-probe (LEAP) tomograph with a picosecond ultraviolet (wavelength = 355 nm) laser at a sample temperature of 25 K, 30-50 pJ laser energy, 200 kHz pulse repetition rate, and a detection rate of 0.05 ions $pulse^{-1}$.

3 Analysis Methods and Results

3.1 Compositions and Microstructure

The measured compositions of the five alloys investigated are listed in Table 1. Compositions were determined by 3-D APT analyses of the solutionized samples for which the compositions are calculated

by dividing the number of atoms of species *i* by the total number of atoms in the reconstructed volume. The error is recorded as 2σ, where σ is calculated through counting statistics as $\sqrt{C_i(1-C_i)/N_{Total}}$ [39]; where C_i is the concentration of species *i,* and N_{Total} is the total number of atoms present in the volume and 2σ is a measure of the scatter in the data. The compositions measured among buttons are in good agreement with the nominal target composition of Co-9.5Al-7.5W-X, where the standard deviation in the Al and W concentrations varied by 0.14 and 0.12 at. %, respectively. In addition to composition, the mean γ'($L1_2$)-precipitate radius, <R>, and the mean γ'($L1_2$)-precipitate volume fraction, ϕ, are listed in Table 1. Each alloy has similar <R> values of ~40 nm independent of alloy composition. The mean grain diameter, <D>, was determined to be <D> = 1.5 ± 0.5 mm for all alloys. The additions of B and Zr were chosen within ranges commonly found in Ni-base superalloys: 0.005-0.5 at. % B and 0.01-0.05 at. % Zr [20-24].

[Table 1 here]

GB triple junctions are delineated with fine dashed white lines within SEM micrographs of the ternary Co-9.5Al-7.5W alloy (Fig. 1a), the two quaternary 0.01B and -0.05Zr alloys (Fig. 1c and d), and the quinary 0.005B-0.05Zr alloy (Fig. 1e) after aging for 16 h at 900 °C. Within the spatial resolution of the SEM, these alloys have no discernable minor phases at the GBs and consist entirely of a γ(f.c.c.) plus γ'($L1_2$) structure without PDZs. In contrast, the GB triple junction in the quaternary 0.05B alloy (Fig. 1b) consists of micron-sized borides and CoAl(B2)-precipitates with a grain interior containing a γ(f.c.c.) plus γ'($L1_2$) microstructure. This structure is similar to those of the alloys cast by Bauer *et al.* [17, 20]. For the 0.05B alloy, the borides have an average width perpendicular to the GB of 0.45 ± 0.15 μm with a PDZ width of 0.75 ± 0.12 μm adjacent to the borides. For comparison, Bauer *et al.* report a 0.5 μm boride width and 1.5 μm PDZ for a comparable aging condition.

[Fig. 1 Here]

3.2 Room Temperature Mechanical Properties of the Aged Alloys

Additions of B and Zr to the ternary Co-9.5Al-7.5W alloy have a negligible impact on the 0.2% yield strength at room temperature (Fig. 2a). With the exception of the 0.05B alloy, the aged alloys exhibit yield strengths that range from 594 to 618 MPa and are statistically equivalent. The 0.05B alloy has a 6 % smaller yield stress value of 564 ± 15 MPa. This discrepancy may be due to the formation of PDZs in the presence of micron-sized borides at the GBs or the alloy's coarse grains, as a limited number of grain orientations are sampled in a single compression test.

[Fig. 2 Here]

Vickers microhardness, which is often used as a proxy for yield stress, was measured for all samples. The microhardness values range from 2.91 to 3.07 GPa and are within the 2σ error of one another (Fig. 2b). Because microhardness is measured within only one grain at a time, the GB properties should not affect the results. Therefore, since B and Zr segregate at GBs, it is anticipated that the microhardness of the grain interior should be similar for all the alloys, even though the yield stress values vary somewhat among samples, which is observed in our alloys.

3.3 Compressive Creep Deformation

Compression creep experiments were performed on all alloys at 850 °C (Fig. 3). The apparent stress exponent, n, was calculated by taking the natural log of the power-law creep equation:

$$\dot{\varepsilon} = A\sigma^n \exp\left(\frac{-Q}{R_g T}\right) \quad (1)$$

where $\dot{\varepsilon}$ is the secondary steady-state strain rate, A is a constant, σ is the applied stress, n is the apparent stress exponent, Q is the activation energy, R_g is the ideal gas constant, and T is the absolute temperature. The total time spent under stress, total strain, stress range, and stress exponent are presented in Table 2.

[Fig. 3 Here]

Creep results obtained by Bauer *et al.* [17] for the ternary Co-9Al-9W alloy (1 data point) and Co-9Al-9W-0.12B alloy (5 data points) are also plotted for comparison (Fig. 3). The apparent stress exponent n is labeled for each alloy and was determined using the power-law creep equation (Eq. 1). In the case of the ternary Co-9.5Al-7.5W alloy, the 105 MPa data point was not used to determine the n value. This is because the secondary minimum strain rate measured at 105 and 125 MPa remained constant at 1.5×10^{-9} s^{-1}, implying that the actual strain rate at 105 MPa was less than the resolution of the LVDT (linear variable differential transformer). In most cases, the strain was less than 3.5 % before the onset of failure by GB fracture as measured by a rapid increase in the strain rate. It is apparent from Fig. 3 that the additions of 0.01B or 0.05Zr do not enhance significantly the creep resistance of the ternary Co-9.5Al-7.5W alloy at higher stresses, and the quaternary alloys actually yield a higher minimum strain rates at lower stress values. The stress exponents of 6.0 and 5.4 measured for 0.01B and Co-9.5Al-7.5W-0.005B-0.05Zr alloys, respectively, are smaller than the 9.9 value measured for our ternary Co-9.5Al-7.5W alloy. The minimum strain rate of a Co-9Al-9W alloy discussed by Bauer *et al.*, at a stress of 250 MPa, is $\sim 5 \times 10^{-7}$ s^{-1} [17]. For comparison, our quaternary 0.01B and 0.05Zr alloys have a minimum strain rate of 3×10^{-7} s^{-1} and 2.5×10^{-7} s^{-1} at applied stresses of 264 and 230 MPa, respectively, while our Co-9.5Al-7.5W alloy exhibits a strain rate of 3.5×10^{-7} s^{-1} at 234 MPa. Conversely, the quinary 0.005B-0.05Zr alloy demonstrates a decrease by nearly an order of magnitude in strain rate, at all stresses, compared to the above three alloys, implying that that the simultaneous addition of B and Zr has a greater effect than incorporating them individually. The 0.05B alloy, which is the only alloy containing micron-sized borides at the GBs, exhibits

the best creep properties. Its minimum strain rates are greater by a factor 2 to 5 as compared to that of the Co-9Al-9W-0.12B alloy [17], which may be due to the smaller B and W concentrations in the former, leading to reduced boride and γ' volume-fractions, respectively.

[Table 2 Here]

3.4 Atom-Probe Tomographic Analyses of Grain Boundary Compositions in 0.01B, 0.05B, and 0.005B-0.05Zr Containing Alloys

3.4.1 Composition of Grain Boundary Borides

Klein *et al.* have hypothesized that the GB borides in Co-Al-W-B are W_5B_3 [28] without measurement of their composition or crystal structure; no such measurement has been reported to our knowledge. In this research, APT was used to measure the composition across a GB boride/ CoAl(B2)-precipitate interface (Fig. 4a) extracted from the 0.05B sample. A proximity histogram [40] corresponding to an isoconcentration surface of 2 at. % B across this interface displays the atomic concentrations of Co, Al, W, and B (Fig. 4b). The Al concentration decreases precipitously from ~40 to 0 at. % in the CoAl(B2)-phase to the boride-phase until the boride is essentially depleted of Al. Conversely, W and B are measured to partition strongly to the boride phase. The composition of the CoAl(B2) phase is Co-36.5Al-2.4W at. %, while the composition of the boride phase is Co-38.6W-23.5B at.%. Both values, with 2σ errors in composition, are summarized in Table 3. The segregation of W to the GB in the 0.05B alloy explains PDZ formation in that as W diffuses from the matrix to GBs to create borides, the regions near GBs become depleted in these elements. Thus, the local composition around the borides shifts toward the γ(f.c.c.)-phase field and the γ'($L1_2$)-precipitates dissolve into the matrix.

[Table 3 Here]

[Fig. 4 Here]

3.4.2 Grain Boundary Segregation of B and Zr in the 0.01B and 0.005B-0.05Zr Alloys

One dimensional concentration profiles across GBs of the 0.01B and 0.005B-0.05Zr alloys were measured via a technique similar to that described in the literature [41, 42] utilizing a dual-beam FIB microscope lift-out process with subsequent APT analyses (Fig. 5). The concentration profiles were measured at a 0.2 nm step size from cylindrical region of interest with areas of 475 nm^2 and 600 nm^2 for the 0.01B (Fig. 6a) and 0.005B-0.05Zr (Fig. 6b) alloy, respectively. The B isoconcentration surface is taken to represent a GB, because it is known that B segregates at GBs [28] in Co-base superalloys.

[Fig. 5 Here]

The peak B concentration at a GB in 0.01B is 1.03 ± 0.11 at. %, which is 100 times greater than the 0.01 at. % bulk concentration. The peak B and Zr concentrations at a GB in 0.005B-0.05Zr are 0.89 ± 0.29 at. % B and 0.99 ± 0.33 at. % Zr and correspond to factors of 200 and 20 times greater than the bulk concentration. In both alloys, the B concentration is undetectable, within error, in the matrix. This also is true for Zr in the 0.005B-0.05Zr alloy.

[Fig. 6 Here]

GB segregation is quantified by calculating the Gibbsian interfacial excess at a GB, Γ_i, where the subscript *i* indicates the atomic species [43]:

$$\Gamma_i = (N_i^{GB} - N_i^0)/A_I; \quad (2)$$

where N_i^{GB} is the number of atoms *i* present at a GB, N_i^0 is the number of *i* atoms in the reference state, and A_I is the area of the interface being sampled [44]. In this case, the reference state is the concentration of the γ(f.c.c.)-matrix phase. The values for Γ_i for Co, Al, W, B, and Zr in the 0.01B and 0.005B-0.05Zr alloys are summarized in Table 3. A negative Γ_i indicates local depletion of a given species at a GB while a positive Γ_i indicates a local excess. In addition to B and Zr, which are expected to segregate at GBs; Co, Al, and W also exhibit segregation or depletion behavior. In 0.01B, Co and Al are depleted at the GB, while W is enriched. The 0.005B-0.05Zr and 0.01B alloys exhibit a similar depletion of Al at their corresponding GBs with values of -4.61 ± 0.54 and -5.38 ± 0.29 Al atoms nm^{-2} respectively. The GB in the 0.01B alloy exhibits, however, almost no segregation of W and is enriched, rather than depleted, of Co. From the Gibbs adsorption isotherm the change in interfacial free energy due to segregation is calculated using the integral method formulated by Blum *et al.* [45]:

$$\Delta E_i = \sum_{j=1}^{N} - \left(C_i^m(j) - C_i^0(j)\right) \Delta x k_b T ln\left(\frac{C_i^m(j)}{C_i^0(j)}\right) \quad (3)$$

where ΔE_i is the change in the interfacial free energy due to segregation, j is the index of the bins of the concentration profile, N is the total number of bins, Δx is the bin width of the concentration profile, k_B is Boltzmann's constant, T is temperature (K), $C_i^m(j)$ is the local measured concentration of species *i*, and $C_i^0(j)$ is the reference concentration, taken to be the γ(f.c.c.)-matrix concentration of species *i* [46]. The ΔE_i for each species is given in Table 4. Boron and Zr segregation result in much larger values of ΔE_i than do Co, Al, or W. Boron segregation results in a decrease of ΔE_i of 363 ± 47 mJ m^{-2} in the 0.01B alloy and similarly B plus Zr co-segregation leads to a reduction in ΔG_i of 320 ± 99 mJ m^2 in the 0.005B-0.05Zr alloy.

[Table 4 Here]

3.5 Grain Boundary Microstructure After Creep at 850 °C

The microstructure of the crept samples was imaged to assist in ascertaining the cause of failure during compressive creep at 850 °C (Fig. 7). The samples were crept to the initial stages of compressive failure in which the strain rate begins transitioning from linear steady-state creep to accelerated deformation. The microstructure of areas at and near the GBs in each of the alloys after creep testing are starkly different from GBs of the alloys prior to creep (Fig. 7). GBs located in the interior of the Co-9.5Al-7.5W alloy (Fig. 7a) were observed to have 0.5-4 μm wide PDZs containing only the γ(f.c.c.)-phase as well as CoAl(B2)-precipitates, not present in the untested aged alloy and large coarsened γ'($L1_2$)-precipitates. The stress-time history varies with each sample, so the resulting microstructures are not directly comparable.

Differences in GB microstructure were also observed for the 0.05B alloy. The semi-continuous GB borides present prior to creep testing (Fig. 1b) are no longer present after creep (Fig. 7b). The regions around the GBs now consists primarily of a γ(f.c.c.)-phase PDZ, where the borides and other minor phases are irregularly dispersed throughout the PDZ. The γ'($L1_2$)-precipitates adjacent to the PDZ have not coarsened in contrast to the other alloys. The occasional Co_3W($D0_{19}$)- and CoAl(B2)- precipitates were observed within the PDZ, where the average compositions were measured from 7-10 particles with EDS to be Co-39.1W and Co-35.9Al-3.0W at. %, respectively.

The regions around GBs in the crept 0.01B alloy (Fig. 7c) are comparable to those observed for the crept Co-9.5Al-7.5W alloy. These regions contain elongated portions of coarsened γ'($L1_2$)-precipitates as well as regions devoid of precipitates, leading to wide PDZs between adjacent grains. GB precipitation

was not observed in the aged 0.01B alloy; CoAl(B2)-precipitates and W-rich borides were found, however, in regions with coarsened γ'($L1_2$)-precipitates in the crept alloy.

The Zr containing alloys also exhibit changes in microstructure around GBS after creep. Compared to all alloys, the 0.05Zr alloy (Fig. 7d) exhibits the most changes; as shown in Fig. 7d, many $Co_3W(D0_{19})$, CoAl(B2), and coarsened γ'($L1_2$)-precipitates decorate the region near the GBs, in addition there are pockets of precipitate free γ(f.c.c.)-regions. For the crept 0.005B-0.05Zr alloy (Fig. 7e), the GBs consist primarily of coarsened γ'($L1_2$)-precipitates without additional minor phases with the exception of one instance of a Zr-rich phase observed by wide area survey of the GBs.

[Fig. 7 Here]

4. Discussion

4.1 Ambient Temperature Compressive Properties

The 0.05B alloy contains GB borides with PDZs on either side of the GB. PDZs have been shown to reduce strongly the yield stress in Ni-base superalloys; e.g., by 10-25 % [22]. Being precipitate free, the PDZ serves as an area where dislocations can be created and glide more readily than in the bulk of the alloy, and where γ'($L1_2$)-precipitates are present to inhibit the migration of dislocations. The Co-9.5Al-7.5W, 0.01B, 0.05Zr, and 0.005B-0.05Zr alloys have similar yield stresses indicating that B and Zr have no effect on the room temperature yield strength when GB precipitation is absent.

4.2 Creep at 850 °C

The creep results (Fig. 3) demonstrate that GB segregants range from having no effect to having an appreciable improvement of the creep behavior of Co-base superalloys. The alloy containing 0.05B exhibited the strongest increase in creep strength in these alloys, which is attributed to the formation of GB borides. The 0.01B and -0.05Zr alloys, in contrast, show no improvement, which differs from Ni-base

alloys, where the presence of 0.005-0.1 at. % B, at a level insufficient for boride formation, is adequate for strengthening GBs between 650-980 °C at stresses between 35-550 MPa [23, 25, 32].

GB borides increase creep strength in similar Co-9Al-9W-X superalloys [17, 20]. To date, a description of the cause of the dramatic increase of creep strength due to the presence of GB borides has not been sufficiently explained. Increased GB strength and cohesion is often cited as the reason for increased creep strength, however if GB strengthening is the only mechanism that borides contribute to, the boride free alloys should creep via GB sliding indicated by a creep stress exponent of n = 2. The stress exponents of boride free alloys presented herein are between 5.4-9.9, indicating creep by dislocation movement. A possible explanation may be that the borides serve a dual strengthening role. The presence of borides increases creep life by improving GB cohesion and improves creep strength by stabilizing GBs, thereby protecting the GBs from precipitation of deleterious phases. Postmortem SEM analyses of GBs, Fig. 7, shows that the microstructure of regions near GBs contain large PDZs often with $Co_3W(D0_{19})$, CoAl(B2), and coarsened $\gamma'(L1_2)$-precipitates. These regions likely serve as areas of easy dislocation glide, thereby lowering the creep strength. In alloys with GB borides, regions near GBs degrade at higher stresses than GBs in boride free alloys.

The addition of 0.01B and 0.05Zr, individually, does not have a significant impact on the creep strength of the Co-9.5Al-7.5W-X alloy; the simultaneous addition of 0.005B and 0.05Zr improves creep resistance, indicating a synergistic effect. The exact mechanism, which does not rely on borides, is unknown, and future research is required to study GBs correlatively utilizing TEM and APT. One possible explanation is that, because combined B and Zr GB segregation appears to reduce W segregation to GBs (Fig. 6) deleterious brittle phase such as $Co_3W(D0_{19})$ are unable to form thereby making the GBs in B-Zr-containing alloys more stable.

4.3 Implications of Zr Segregation at Grain Boundaries in the 0.005B-0.05Zr Alloy

Segregation of B and Zr to the GBs strengthens GBs in Ni-base superalloys [23, 25, 32], but GB segregants in the Co-base superalloys have not been studied in detail. Zirconium additions combined with B have a positive influence on the creep properties of polycrystalline Co-Al-W alloys (Fig. 3). Segregation of B and Zr to GBs in the 0.005B-0.05Zr alloy implies that zirconium borides, rather than tungsten borides, may form at GBs once the GBs have achieved the maximum concentrations permitted by the Gibbs adsorption isotherm. This would decrease, and possibly even eliminate, W segregation at the GBs, hence eliminating the PDZs that form in alloys containing only B for GB strengthening. Enthalpies of formation [47-51] for different Co, Al, W, and Zr borides are compiled in Table 5. ZrB_2 has the most negative enthalpy of formation of any of the other compounds, followed by the W, Co, and Al borides, which is consistent with the strong Zr-B bonding. Therefore, it is possible that increasing the Zr and B concentrations beyond those studied herein could further strengthen the GBs and improve creep properties through the formation of Zr-rich borides while limiting PDZ width which occurs due the formation of W-rich borides.

[Table 5 Here]

4.4 Grain Boundary Failure

In all events of failure in this work the cause was observed to be intergranular fracture, which emphasizes the need for GB strengtheners in polycrystalline Co-base superalloys. SEM of the post-crept microstructures (Fig. 7) presents different examples of GB microstructures, which typically includes heavily coarsened $\gamma'(L1_2)$-precipitates and less coarse $Co_3W(D0_{19})$ and CoAl(B2) particles, which have a much different appearance than GBs in the aged condition (Fig. 1). Discerning whether precipitation at the GBs is the result or the cause of failure is not obvious. In the former case, other systems exhibit GB precipitation caused by GB sliding and fracture [52]. In the latter case, there are many articles challenging the stability of the γ(f.c.c.) plus $\gamma'(L1_2)$ phase field in the Co-Al-W system [53-55]. In a situation where

the γ(f.c.c.) plus γ'($L1_2$)-phase field is metastable or barely stable, GBs in the presence of stress may serve as a heterogeneous nucleation region for formation of the stable, but undesirable $Co_3W(D0_{19})$ and CoAl(B2) phases.

5 Summary

One ternary Co-9.5Al-7.5W at. %, three quaternary Co-9.5Al-7.5W-X at. % (where X = 0.05B, 0.01B, 0.05Zr), and one quinary Co-Al-W-X at. % (with X = 0.005B+0.05Zr) alloys were cast and aged to obtain a γ(f.c.c.) plus γ'($L1_2$) microstructure. The GB segregation behavior and mechanical properties of B and Zr containing Co-base superalloys were characterized via 3-D atom-probe tomographic analyses, compression testing, and high-temperature compression creep. The following conclusions are reached:

- B and Zr were shown to segregate strongly to GBs in the Co-9.5Al-7.5W-0.01B at. % and Co-9.5Al-7.5W-0.005B-0.05Zr at. % alloys. Simultaneous addition of 0.005B and 0.05Zr to Co-9.5Al-7.5W at. % improved creep strength over the baseline ternary alloy without forming GB borides.
- Boron segregation at GBs leads to large W-rich borides in Co-9.5Al-7.5W-0.05B at. %, but not in Co-9.5Al-7.5W-0.01B at. % alloy. Tungsten diffuses from the matrix to the GBs to form the borides, leaving the matrix W-deficient, thus moving the local composition from the γ(f.c.c.) plus γ'($L1_2$) to the γ(f.c.c.) phase-field and creating a γ'($L1_2$)-precipitate denuded zone (PDZ) near the GBs.
- GB borides have a strong effect on the creep strength by strengthening the GBs as exhibited by a pronounced decrease in the minimum steady-state strain rate by two orders of magnitude for a given stress when compared to Co-9.5Al-7.5W at. %.

- The PDZ acts a soft region for easy dislocation movement, with the effect that the yield strength at room temperature decreases from 598 MPa in the base Co-Al-W to 564 MPa in the Co-9.5Al-7.5W-0.05B at. %alloy containing grain-boundary borides.
- A GB boride in the Co-9.5Al-7.5W-0.05B at. % alloy was measured for the first time and was found to have a composition of Co-38.62W-23.49B at. %, with nearly equal amounts of Co and W, and no Al.
- Regions near the GBs of crept alloys exhibit a large amount of precipitation, primarily comprised of $Co_3W(D0_{19})$ (Co-39.1W at. %), CoAl(B2) (Co-36.5Al-2.4W at %), and coarsened $\gamma'(L1_2)$-precipitates, plus precipitate depleted zones not observed in uncrept alloys.

Acknowledgments

This research was supported by the US Department of Energy, Office of Basic Energy Sciences (Dr. John Vetrano, grant monitor) through grant DE-FG02-98ER45721. P.J.B. received partial support from NASA Aeronautics Scholarship Program and Fixed Wing project. APT measurements were conducted at the Northwestern University Center for Atom-Probe Tomography (NUCAPT). The APT system was purchased and upgraded with funding from NSF-MRI (DMR-0420532) and ONR-DURIP (N00014-0400798, N00014-0610539 and N00014-0910781) grants. NUCAPT is a shared facility of the Materials Research Center of NU, supported by the National Science Foundation MRSEC Program (DMR-1121262). The authors also gratefully acknowledge the Initiative for Sustainability and Energy at Northwestern (ISEN) for grants to upgrade the capabilities of NUCAPT. This work made use of Northwestern's Materials Research Center funded by the NSF MRSEC program (DMR-112162). TEM research was performed at the Northwestern University Atomic and Nanoscale Characterization Experimental (NUANCE) Center. The authors would like to thank research associate professor D. Isheim for

managing NUCAPT, Dr. S.-I. Baik for assistance with transmission electron microscopy, Drs. Dave Ellis and Cheryl Bowman for assistance with creep experiments, Mr. Grant Feichter and Jesse Bierer for arc melting and heat treating, and Dr. Tim Gabb for helpful discussions.

References

[1] R.C. Reed. The Superalloys, Cambridge University Press, New York, 2006.

[2] C.T. Sims, N.S. Stoloff, W.C. Hagel. Superalloys II, John Wiley & Sons Inc, New York, 1987.

[3] P. Caron, T. Khan. Evolution of Ni-Based Superalloys for Single Crystal Gas Turbine Blade Applications, Aerosp. Sci. Technol. 3 (1999) 513-523.

[4] T.M. Pollock, A.S. Argon. Creep Resistance of CMSX-3 Nickel Base Superalloy Single Crystals, Acta Metall 40 (1992) 1-30.

[5] M. Durand-Charre. The Microstructure of Superalloys, Gordon and Breach Science Publishers, Amsterdam, 1997.

[6] Haynes International. Haynes 188 Alloy. Standard Products by Brand or Alloy Designation.

[7] J. Sato, T. Omori, K. Oikawa, I. Ohnuma, R. Kainuma, K. Ishida. Cobalt-Base High-Temperature Alloys, Science 312 (2006) 90-91.

[8] F. Pyczak, A. Bauer, M. Göken, U. Lorenz, S. Neumeier, M. Oehring, J. Paul, N. Schell, A. Schreyer, A. Stark, F. Symanzik. The Effect of Tungsten Content on the Properties of L12-Hardened Co–Al–W alloys, J Alloys Compd 632 (2015) 110-115.

[9] H.-Y. Yan, V.A. Vorontsov, D. Dye. Alloying Effects in Polycrystalline γ′ Strengthened Co–Al–W Base Alloys, Intermetallics 48 (2014) 44-53.

[10] Y.M. Eggeler, M.S. Titus, A. Suzuki, T.M. Pollock. Creep Deformation-Induced Antiphase Boundaries in L12-Containing Single-Crystal Cobalt-Base Superalloys, Acta Mater 77 (2014) 352-359.

[11] M.S. Titus, A. Suzuki, T.M. Pollock. Creep and Directional Coarsening in Single Crystals of New γ–γ′ Cobalt-Base Alloys, Scr Mater 66 (2012) 574-577.

[12] M.S. Titus, A. Suzuki, T.M. Pollock. High Temperature Creep of New L12-Containing Cobalt-Base Superalloys, Superalloys 12 (2012) 823-831.

[13] A. Suzuki, T.M. Pollock. High-Temperature Strength and Deformation of γ/γ′ Two-Phase Co–Al–W-Base Alloys, Acta Mater 56 (2008) 1288-1297.

[14] A. Suzuki, G.C. Denolf, T.M. Pollock. Flow Stress Anomalies in γ/γ′ Two-Phase Co–Al–W-Base Alloys, Scr Mater 56 (2007) 385-388.

[15] F. Xue, H.J. Zhou, Q.Y. Shi, X.H. Chen, H. Chang, M.L. Wang, Q. Feng. Creep Behavior in a γ′ Strengthened Co–Al–W–Ta–Ti Single-Crystal Alloy at 1000°C, Scr Mater 97 (2015) 37-40.

[16] A. Bauer, S. Neumeier, F. Pyczak, M. Goken. Microstructure and Creep Strength of Different γ/γ′-Strengthened Co-Base Superalloy Variants, Scr Mater 63 (2010) 1197-1200.

[17] A. Bauer, S. Neumeier, F. Pyczak, R.F. Singer, M. Göken. Creep Properties of Different γ′-Strengthened Co-Base Superalloys, Mater Sci Eng A 550 (2012) 333-341.

[18] I. Povstugar, P.-P. Choi, S. Neumeier, A. Bauer, C.H. Zenk, M. Göken, D. Raabe. Elemental Partitioning and Mechanical Properties of Ti- and Ta-Containing Co–Al–W-Base

Superalloys Studied by Atom Probe Tomography and Nanoindentation, Acta Mater 78 (2014) 78-85.

[19] K. Tanaka, M. Ooshima, N. Tsuno, A. Sato, H. Inui. Creep Deformation of Single Crystals of New Co–Al–W-Based Alloys with fcc/L12 Two-Phase Microstructures, Philos Mag 92 (2012) 4011-4027.

[20] A. Bauer, S. Neumeier, F. Pyczak, M. Göken. Creep Strength and Microstructure of Polycrystalline γ′ – Strengthened Cobalt-Base Superalloys, Superalloys 12 (2012) 695-703.

[21] K. Shinagawa, T. Omori, K. Oikawa, R. Kainuma, K. Ishida. Ductility Enhancement by Boron Addition in Co–Al–W High-Temperature Alloys, Scr Mater 61 (2009) 612-615.

[22] T. Krol, D. Baither, E. Nembach. The Formation of Precipitate Free Zones Along Grain Boundaries in a Superalloy and the Ensuing Effects on its Plastic Deformation, Acta Mater 52 (2004) 2095-2108.

[23] T.J. Garosshen, T.D. Tillman, G.P. McCarthy. Effects of B, C, and Zr on the Structure and Properties of a P/M Nickel Base Superalloy, Metall Trans A 18A (1987) 69-77.

[24] T.H. Chuang. The Mutual Effects of Boron, Zirconium, and Aluminum on Grain Boundary Segregation in Ni3Al Intermetallic Compounds, Mat Sci Eng A 141 (1991) 169-178.

[25] E.S. Huron, K.R. Bain, D.P. Mourer, J.J. Schirra, P.L. Reynolds, E.E. Montero. The Influence of Grain Boundary Elements on Properties and Microstructures of P/M Nickel Base Superalloys, Superalloys (2004) 73-81.

[26] L. Klein, B. von Bartenwerffer, M.S. Killian, P. Schmuki, S. Virtanen. The Effect of Grain Boundaries on High Temperature Oxidation of New γ′-Strengthened Co–Al–W–B Superalloys, Corros Sci 79 (2014) 29-33.

[27] L. Klein, S. Virtanen. Corrosion Properties of Novel γ′–Strengthened Co-Base Superalloys, Corros Sci 66 (2013) 233-241.

[28] L. Klein, Y. Shen, M.S. Killian, S. Virtanen. Effect of B and Cr on the High Temperature Oxidation Behaviour of Novel γ/γ′-Strengthened Co-Base Superalloys, Corros Sci 53 (2011) 2713-2720.

[29] L. Klein, A. Bauer, S. Neumeier, M. Göken, S. Virtanen. High Temperature Oxidation of γ/γ′-Strengthened Co-Base Superalloys, Corros Sci 53 (2011) 2027-2034.

[30] W.Z. Wang, H.U. Hong, I.S. Kim, B.G. Choi, H.W. Jeong, M.Y. Kim, C.Y. Jo. Influence of γ′ and Grain Boundary Carbide on Tensile Fracture Behaviors of Nimonic 263, Mater Sci Eng A 523 (2009) 242-245.

[31] F.T. Furillo, J.M. Davidson, J.K. Tien, L.A. Jackman. The Effects of Grain Boundary Carbides on the Creep and Back Stress of a Nickel-base Superalloy, Mater Sci Eng 39 (1979) 267-273.

[32] S. Floreen, J.M. Davidson. The Effects of B and Zr on the Creep and Fatigue Crack Growth Behavior of a Ni-Base Superalloy, Metall Trans A 14A (1983) 895-901.

[33] D.N. Seidman, K. Stiller. An Atom-Probe Tomography Primer, Mater Res Bull 34 (2009) 717-721.

[34] D.N. Seidman. Three-Dimensional Atom-Probe Tomography: Advances and Applications, Annu Rev Mater Sci 37 (2007) 127-158.

[35] C.K. Sudbrack, R.D. Noebe, D.N. Seidman. Direct Observations of Nucleation in a Nondilute Multicomponent Alloy, Phys Rev B 73 (2006) 1-4.

[36] J.C. Russ, R.T. Dehoff. Practical Stereology. 2 ed., Springer, New York, New York, 1986.

[37] B.W. Krakauer, J.G. Hu, S.-M. Kuo, R.L. Mallick, A. Seki, D.N. Seidman, J.P. Baker, R. Loyd. A System for Systematically Preparing Atom-Probe Field-Ion Microscope Specimens for the Study of Internal Interfaces, Rev Sci Instrum 61 (1990) 3390-3398.

[38] B.W. Krakauer, D. Seidman. Systematic Procedures for Atom-Probe Field-Ion Microscopy Studies of Grain Boundary Segregation, Rev Sci Instrum 63 (1992) 4071-4079.

[39] F. Danoix, G. Grancher, A. Bostel, D. Blavette. Standard Deviations of Composition Measurements in Atom Probe Analyses—Part II: 3D Atom Probe, Ultramicroscopy 107 (2007) 739-743.

[40] O.C. Hellman, J.A. Vandenbroucke, J. Rusing, D. Isheim, D.N. Seidman. Analysis of Three-Dimensional Atom-Probe Data by the Proximity Histogram, Microsc Microanal 6 (2000) 437-444.

[41] H. Li, S. Xia, W. Liu, T. Liu, B. Zhou. Atomic Scale Study of Grain Boundary Segregation Before Carbide Nucleation in Ni–Cr–Fe Alloys, J Nucl Mater 439 (2013) 57-64.

[42] S.-I. Baik, M.J. Olszta, S.M. Bruemmer, D.N. Seidman. Grain-Boundary Structure and Segregation Behavior in a Nickel-Base Stainless Alloy, Scr Mater 66 (2012) 809-812.

[43] J.W. Cahn. Thermodynamics of Solid and Fluid Surfaces. In: Johnson WC, Blakely JM, (Eds.). ASM, 1978. p.3-23.

[44] O.C. Hellman, J. Rüsing, J.T. Sebastian, D.N. Seidman. Atom-by-Atom Chemistry of Internal Interfaces: Simulations and Experiments, Mater Sci Eng C 15 (2001) 13-15.

[45] I.D. Blum, S.-I. Baik, M.G. Kanatzidis, D.N. Seidman. An Integral Method for the Calculation of the Reduction in Interfacial Free Energy Due to Interfacial Segregation, Submitted (January 2016).

[46] A. Biswas, D.J. Siegel, C. Wolverton, D.N. Seidman. Precipitates in Al–Cu Alloys Revisited: Atom-Probe Tomographic Experiments and First-Principles Calculations of Compositional Evolution and Interfacial Segregation, Acta Mater 59 (2011) 6187-6204.

[47] M.J. van Setten, M. Fichtner. On the Enthalpy of Formation of Aluminum Diboride, AlB2, J Alloys Compd 477 (2009) L11-L12.

[48] D. Mirković, J. Gröbner, R. Schmid-Fetzer, O. Fabrichnaya, H.L. Lukas. Experimental Study and Thermodynamic Re-Assessment of the Al–B system, J Alloys Compd 384 (2004) 168-174.

[49] S. Sato, O.J. Kleppa. Enthalpies of Formation of Borides of Iron, Cobalt, and Nickel by Solution Calorimetry in Liquid Copper, Metall Trans B 13 (1982) 251-257.

[50] E.S. Domalski, G.T. Armstrong. Heats of Formation of Metallic Borides by Flourine Bomb Calorimetry In: USAF, (Ed.). Washington D.C. : National Bureau of Standards, 1964.

[51] E.J. Huber, E.L. Head, C.E. Holley. The Heats of Formation of Zirconium Diboride and Dioxide, J Phys Chem 68 (1964) 3040-3042.

[52] J. Wadsworth, O. Ruano, O. Sherby. Denuded Zones, Diffusional Creep, and Grain Boundary Sliding, Metall and Mat Trans A 33 (2002) 219-229.

[53] S. Kobayashi, Y. Tsukamoto, T. Takasugi, H. Chinen, T. Omori, K. Ishida, S. Zaefferer. Determination of Phase Equilibria in the Co-rich Co–Al–W Ternary System with a Diffusion-Couple Technique, Intermetallics 17 (2009) 1085-1089.

[54] Y. Tsukamoto, S. Kobayashi, T. Takasugi. The Stability of γ ’-Co3(Al,W) Phase in Co-Al-W Ternary System, Mater Sci Forum 654-656 (2010) 448-451.

[55] S. Kobayashi, Y. Tsukamoto, T. Takasugi. The Effects of Alloying Elements (Ta, Hf) on the Thermodynamic Stability of γ′-Co3(Al,W) Phase, Intermetallics 31 (2012) 94-98.

Tables Captions:

Table 1: Bulk compositions of the Co-9.5-7.5-X alloys measured utilizing atom probe tomography (APT) and the mean radius, <R>, and volume fraction, ϕ, of the γ'($L1_2$)-precipitates as measured from SEM images. Parenthetical values are the 2σ errors.

Table 2: List of total creep times, total strain, and stress exponent n (with standard error in parenthesis) for all creep tests.

Table 3: The concentration profile at the interface of a boride and CoAl(B2)-phase located at a grain boundary of the Co-9.5-7.5-0.05B alloy as measured with APT.

Table 4: Gibbsian interfacial excess (Γ_i) and the resulting reduction in the Gibbsian interfacial free energy (ΔE) of a grain boundary in the Co-9.5-7.5-0.01B and Co-9.5-7.5-0.005B-0.05Zr alloys, as calculated from the concentration profiles of solute atoms across the grain boundary. The 2σ errors are given in parenthesis.

Table 5: Enthalpies of formation (ΔH_f) of various borides commonly formed with Al, Co, W and Zr.

Table 1: Caption in Table Captions File

Alloy nominal composition Co-9.5Al-7.5W-X (at. %)	Alloy composition as measured by APT (at. %)					<*R*> (nm)	ϕ (%)
	Co	Al	W	B	Zr		
Ternary	Bal.	9.49 (0.02)	7.45 (0.02)	-	-	37 (13)	34 (4)
0.05B	Bal.	9.56 (0.02)	7.50 (0.02)	0.0385 (0.0004)	-	35 (12)	35 (4)
0.01B	Bal.	9.85 (0.02)	7.64 (0.02)	0.0092 (0.0003)	-	36 (12)	37 (5)
0.05Zr	Bal.	9.58 (0.02)	7.40 (0.02)	-	0.0350 (0.0003)	40 (8)	37 (4)
0.005B-0.05Zr	Bal.	9.53 (0.02)	7.66 (0.02)	0.0054 (0.0005)	0.0275 (0.0010)	49 (8)	40 (5)

Table 2: Caption in Table Captions File

Alloy	Sample	Creep Time (h)	Stress Range (MPa)	Total Strain (%)	n
Ternary	1	476	105-235	3.3	9.9 (1.0)
0.05B	1 2 3	195 25 84	221-309 309-398 221-375	2.2 2.2 1.2	7.8 (0.6)
0.01B	1 2 3	121 5 225	176 264 130-226	2.0 3.4 2.1	6.0 (0.3)
05Zr	1 2	101 248	153-230 127-184	3.6 2.6	5.4 (0.4)
0.05Zr-0.005B	1 2	200 73	176-220 220-308	2.09 1.61	7.6 (0.5)

Table 3: Caption in Table Captions File

Element	Concentration ± 2σ (at. %)	
	Boride	B2
Co	37.05 ± 2.44	60.61 ± 1.38
Al	< 0.01	36.49 ± 1.41
W	38.62 ± 2.71	2.40 ± 0.41
B	23.49 ± 2.13	< 0.01

Table 4: Caption in Table Captions File

Alloy	Interfacial Excess Γ_i (atoms nm^{-2})					ΔE (mJ m^2)				
	Co	Al	W	B	Zr	Co	Al	W	B	Zr
0.01B	-3.70 (0.02)	-5.38 (0.29)	4.32 (0.23)	5.57 (1.04)	-	2.30 (0.02)	31.61 (1.77)	40.32 (2.32)	362.54 (47.39)	-
0.005B-0.05Zr	1.22 (0.01)	-4.61 (0.54)	0.48 (0.07)	2.88 (0.81)	2.40 (0.84)	0.55 (0.01)	25.91 (3.15)	2.69 (0.40)	168.26 (77.68)	152.78 (61.89)

Table 5: Caption in Table Captions File

Boride	ΔH_f
	kJ mol^{-1}
AlB_2[47,48]	-8 to -29
Co_2B[49]	-52 to -69
CoB[49]	-62 to -75
W_2B[50]	-84 to -117
W_2B_5[50]	-105 to -188
WB [50]	-50 to -92
ZrB_2 [50,51]	-248 to -323

Figure Captions

Fig. 1: Backscattered electron SEM micrographs of grain boundary triple points separating γ(f.c.c.) plus γ'($L1_2$) grains in: (a) Co-9.5Al-7.5W; (b) -0.05B; (c) -0.01B; (d) -0.05Zr; and (e) -0.005B-0.05Zr at. % alloys after 16 h of aging at 900 °C. Micrographs (a) and (c-e) show similar GB structures devoid of visible GB precipitates, while micrograph (b) exhibits borides (white) and CoAl(B2) (black) precipitates at the GB with adjacent precipitate denuded zones (PDZs).

Fig. 2: (a) Stress vs. strain curves of alloys at room temperature plotted in order of descending 0.2 % yield strength. (b) Plot of 0.2% yield strength shown as vertical blue bars and corresponding Vickers microhardness presented as red points.

Fig. 3: Plot of minimum secondary creep rate vs. applied stress for the Co-9.5Al-7.5W, -0.05B, -0.01B, -0.05Zr, and -0.005B-0.05Zr at. % alloys tested in compression at 850 °C. Alloys are identified by color and symbols representing different samples of the same alloy having different fills. The apparent stress exponent, n, of each alloy is shown at the top-left of each curve. Data from the literature for Co-9Al-9W (one single cross) and Co-9Al-9W-0.12B (multiple x) [17] are included for comparison.

Fig. 4: (a) Atom-probe tomographic reconstruction of a CoAl(B2)/boride interface found at a GB in the Co-9.5Al-7.5W-0.05B at. % alloy; and (b) corresponding proximity histogram concentration profile.

Fig. 5: (a) STEM image of a GB in the Co-9.5Al-7.5W-0.005B-0.05Zr alloy. (b) Atom-probe tomographic nanotip fabricated employing the FIB lift-out technique of the same GB. (c) Atom-probe tomographic 3D reconstruction of the nanotip displayed in (b). A boron (cyan)

isoconcenration surface is used to delineate the two grains. A tungsten (orange) isoconcentration surface is used to designate a γ'($L1_2$)-precipitate at the end of the nanotip.

Fig. 6: Plots of the concentration profiles measured with APT along a γ(f.c.c.)-grain boundary in the Co-9.5Al-7.5W-0.01B (left) and Co-9.5Al-7.5W-0.005B-0.05Zr (right) alloy.

Fig. 7: Backscattered electron SEM micrographs showing different forms of grain boundary precipitation after creep at 850 °C in: (a) Co-9.5Al-7.5W (t = 476 h, σ = 105-235 MPa); (b) Co-9.5Al-7.5W-0.05B (t = 25 h, σ = 309-398 MPa); (c) Co-9.5Al-7.5W-0.01B (t = 121 h, σ = 176 MPa); (d) Co-9.5Al-7.5W-0.05Zr (t=248 h, σ = 127-184 MPa); and (e)Co-9.5Al-7.5W-0.005B-0.05Zr (t = 73 h, σ = 220-308 MPa).

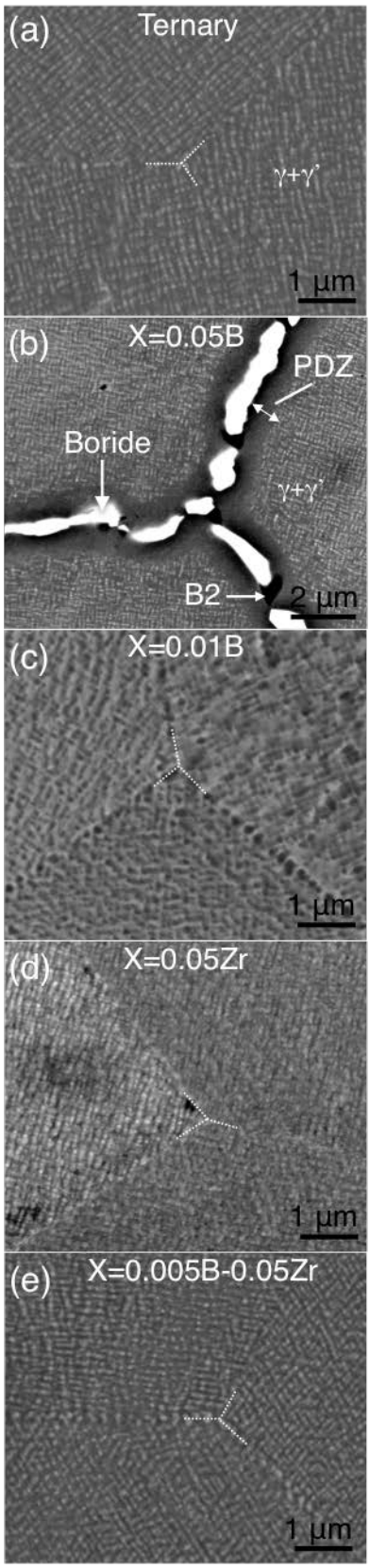
(a)
Ternary
γ+γ'
1 μm
(b)
X=0.05B
PDZ
Boride
γ+γ'
B2
2 μm
(c)
X=0.01B
1 μm
(d)
X=0.05Zr
1 μm
(e)
X=0.005B-0.05Zr
1 μm

Fig. 1:

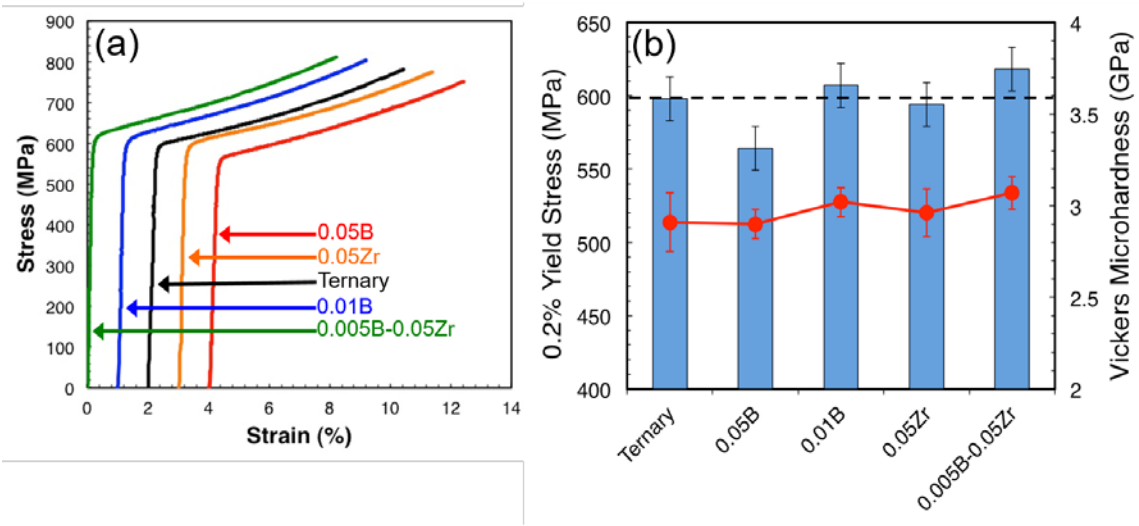

Figure 2:

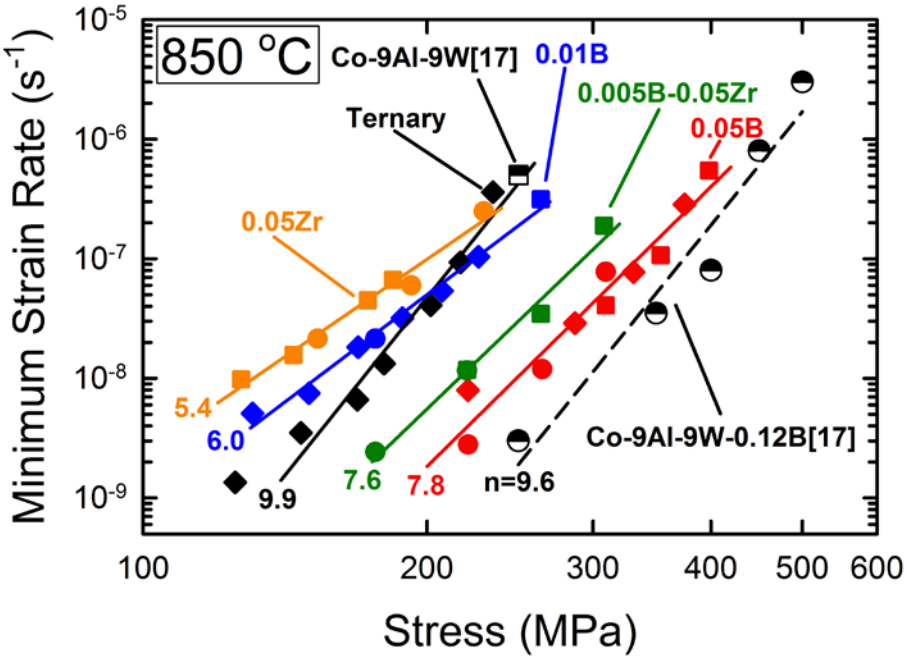

Fig. 3:

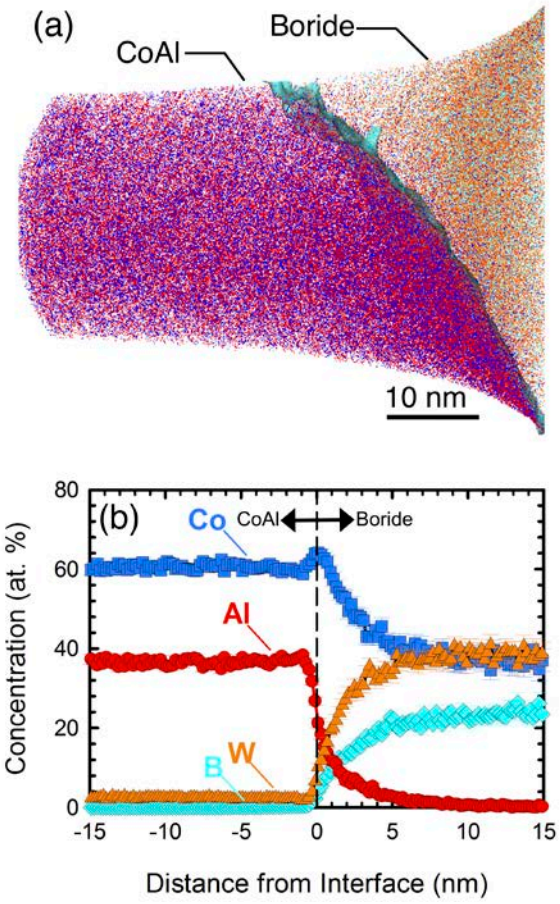
(a)
CoAl
Boride
10 nm
(b)
Co
CoAl
Boride
Al
B
W
Concentration (at. %)
Distance from Interface (nm)
80
60
40
20
0
-15
-10
-5
0
5
10
15

Fig. 4:

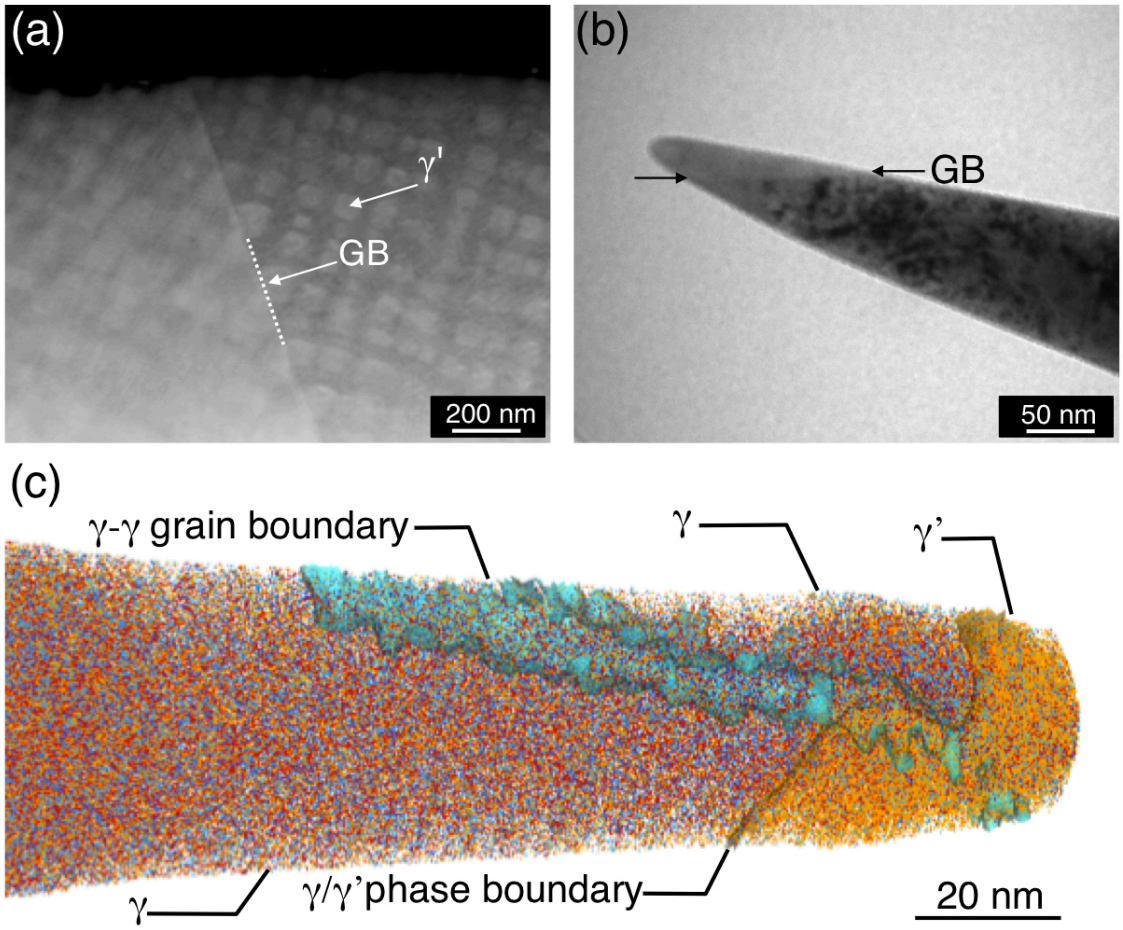
(a)
γ'
GB
200 nm
(b)
GB
50 nm
(c)
γ-γ grain boundary
γ
γ'
γ
γ/γ'phase boundary
20 nm

Fig. 5:

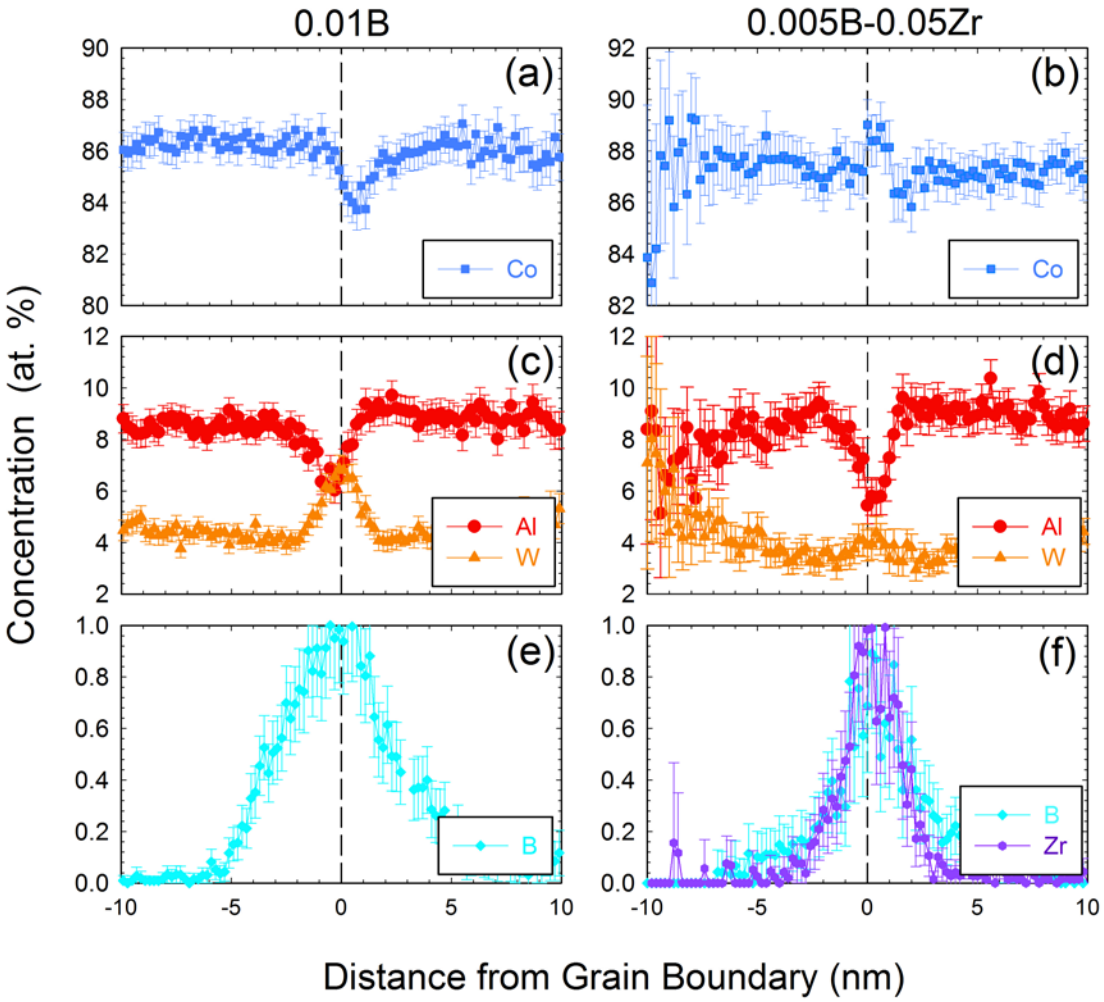
0.01B
0.005B-0.05Zr
(a)
(b)
(c)
(d)
(e)
(f)
Co
Al
W
B
Zr
Concentration (at. %)
Distance from Grain Boundary (nm)

Figure 6:

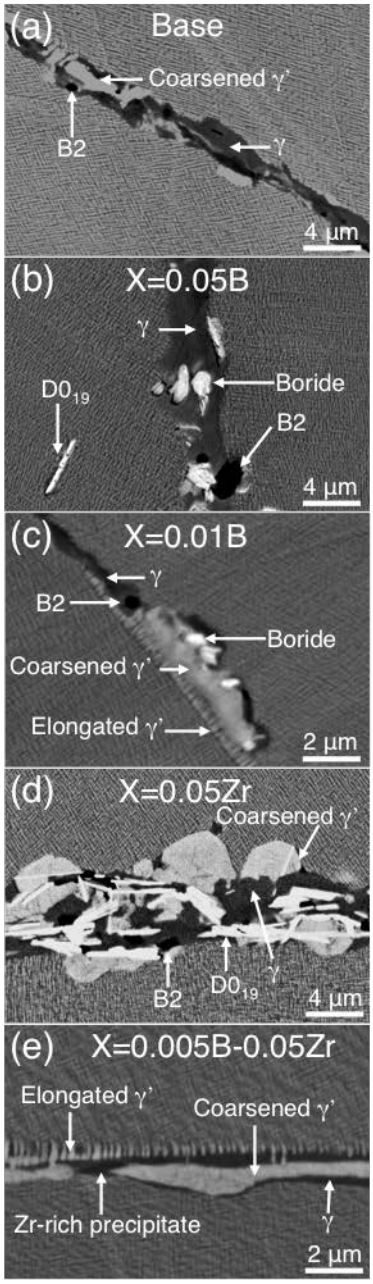
(a)
Base
Coarsened γ'
B2
γ
4 μm
(b)
X=0.05B
γ
Boride
D0$_{19}$
B2
4 μm
(c)
X=0.01B
γ
B2
Boride
Coarsened γ'
Elongated γ'
2 μm
(d)
X=0.05Zr
Coarsened γ'
γ
B2
D0$_{19}$
4 μm
(e)
X=0.005B-0.05Zr
Elongated γ'
Coarsened γ'
Zr-rich precipitate
γ
2 μm

Figure 7: